The Stochastic Modeling of Solidification Structures in Alloy 718 Remelt Ingots

Laurentiu Nastac, Suresh Sundarraj, Kuang-O Yu, and Yuan Pang

A stochastic numerical approach was developed to model the formation of grain structure and secondary phases during the solidification of nickel-based alloy 718 remelt ingots. The significance of the present stochastic approach is that the simulated phases can be directly compared with actual phases from experiments at two different scales: grain characteristics can be visualized at the macroscale, while the amount, size, and distribution of secondary phases can be viewed at the microscale. The computer becomes a "dynamic metallographic microscope." Stochastic modeling was applied to simulate the formation of solidification phases (γ primary phase and NbC and eutectic γ-Laves secondary phases) during the solidification of vacuum-arc-remelted and electroslag-remelted alloy 718 ingots. Modeling results, such as pool profile, grain-growth pattern, grain structure (both columnar and equiaxed grains), columnar-to-equiaxed transition, grain size, and secondary dendrite arm spacing, as well as amount, size, and location of both eutectic γ-Laves and NbC phases compared well with experimental data for cast alloy 718. This research demonstrates that the stochastic approaches are relatively fast, comprehensive, and more accurate than the deterministic approaches in predicting the solidification characteristics of remelt ingots and are mature enough to be used effectively by the metal industry for process development and optimization.

INTRODUCTION

Quality is one of the major concerns in the manufacture of high-performance superalloy components (turbine and compressor discs) for aerospace and other commercial applications. The materials for these components are made by secondary remelting processes, such as vacuum arc remelting (VAR) and electroslag remelting (ESR), which involve a continuous-casting operation to produce an ingot. The quality of the cast ingots produced by these processes is governed by grain structure formation (columnar and equiaxed morphologies and the columnar-to-equiaxed transition [CET]) and micro-/macrosegregation phenomena, such as the formation of Laves phases, carbides, and freckles for alloy 718.

Process modeling has become a viable tool for optimizing the ESR and VAR processes. A comprehensive modeling approach for simulating ingot solidification phenomena in secondary remelting processes is depicted in Figure 1.[1–3] Based on process- and material-parameter input data, the deterministic model performs macroscopic mass, heat transfer, fluid flow, electromagnetic, and species-transport computations to provide temperature, velocity, and concentration-field output. From the macroscopic temperature field, the pool profile and pool size as well as the shape and size of the mushy region can be determined. In addition, macrosegregation-related defects, such as freckles and tree-ring patterns, can be obtained from the concentration field. A stochastic model uses the results from the macromodel to predict the grain-structure evolution of solidifying ingots. It also computes grain size, CET, and microsegregation-related defects, such as the amount and size of secondary phases (Laves phases and NbC in alloy 718).

The stochastic model is useful because the simulated structures can be directly compared with actual structures obtained from experiments; the computer becomes a dynamic metallographic microscope. The stochastic model is comprehensive because the competition between nucleation and grain-growth kinetics of various phases is considered. Furthermore, grain impingement is directly accounted for in the model. In fact, the stochastic predictability of alloy solidification is one of the three greatest findings of the twentieth century, as quoted by Gleick:[4] "Twentieth-century science will be remembered for just three things: relativity, quantum mechanics, and chaos. Relativity eliminated the Newtonian illusion of absolute space and time; quantum theory eliminated the Newtonian dream of a controllable measurement process; and chaos eliminates the Laplacian fantasy of deterministic predictability." Alloy solidification is an ordered chaotic process[4] that can be simulated only through a stochastic modeling approach.

THE STOCHASTIC MODEL

The stochastic model consists of three components: a deterministic macroscopic approach for modeling heat transfer, mass transfer, and fluid flow during the ingot solidification process; a stochastic microscopic approach for simulating the evolution of grain structure; and a stochastic microscopic approach for simulating the evolution of secondary phases.

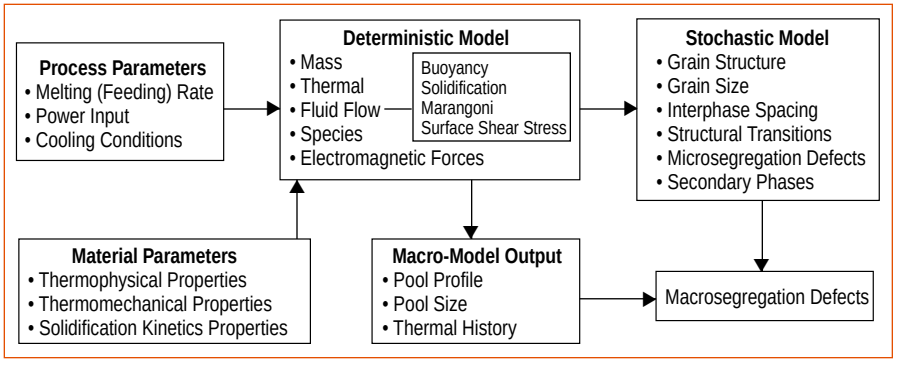

Figure 1. A flow diagram showing the modeling requirements for secondary remelting processes.

A moving-grid, fully implicit, control-volume method was developed to describe the transient macrotransport phenomena in solidifying continuously cast ingots. The model was implemented in COMPACT™.[5] A detailed description of this macromodel is described in References 2 and 3. For an axisymmetric geometry, the appropriate heat-transfer boundary conditions for these processes include symmetry at the ingot center,

convection and radiation at the ingot edge and bottom, and process-specific boundary conditions at the ingot top to account for the heat input (due to metal flow into the domain) and heat loss (due to radiation from the top surface).

The present stochastic approach differs from the classical "cellular automata" technique[6–13] in that it uses thermal history results from the deterministic model described previously.[1,2,14] The development of the stochastic model for grain-structure evolution is described in detail in References 1, 2, 7, and 8. This description includes nucleation and growth kinetics, growth anisotropy, and grain selection mechanisms. The required input data for performing stochastic calculations include the local cooling rates calculated at the liquidus and solidus temperatures, the local time-dependent temperature gradients in the mushy zone calculated at the liquidus and solidus temperatures, and the local solidification start and end times. These data are provided by a deterministic macroscopic model for each computational cell. Local cooling rates calculated at the liquidus temperature are used to compute the nucleation parameters. Local average cooling rates and time-dependent temperature gradients in the mushy zone are used to compute the grain-growth parameters.

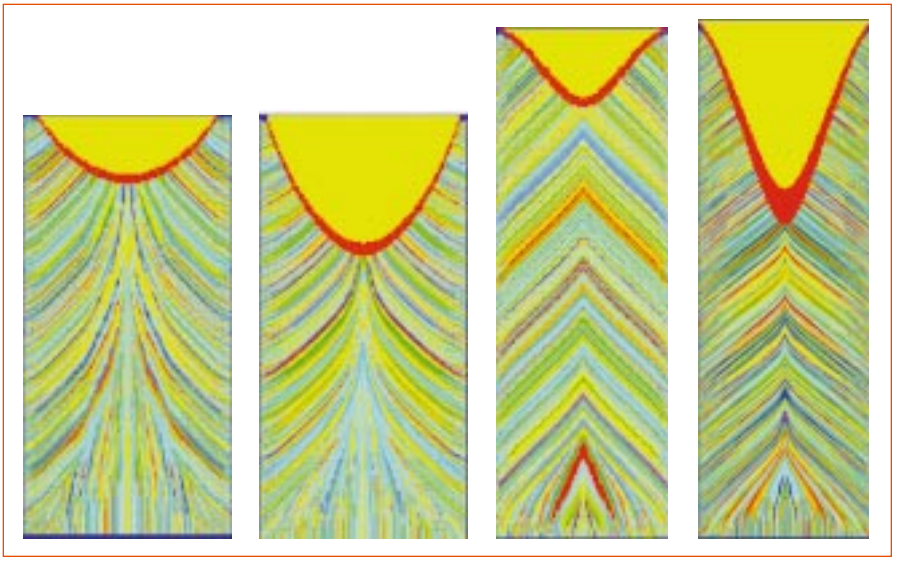

Figure 2. A comparison between simulated structures of alloy 718 remelt ingots (a) VAR, 172 kg/h, D = 508 mm, H = 2 D, (b) VAR, 327 kg/h, D = 508 mm, H = 2 D, (c) ESR, 272 kg/h, D = 432 mm, H = 3 D, (d) ESR, 591 kg/h, D = 432 mm, H = 3 D.

At least three grain morphologies are encountered during the solidification of remelt ingots: equiaxed grains; columnar grains solidified under a variable gradient/velocity (G/V) ratio; and columnar grains solidified under a relatively constant G/V ratio, where G and V are the local temperature gradient and solid/liquid (S/L) interface velocity of the mushy region, respectively. All morphologies, as well as the CET, are driven more or less by the same solidification mechanism (i.e., the nucleation and growth competition of various phases in the mushy region). The stochastic models for equiaxed and columnar grains solidified under a variable G/V ratio are described in References 7 and 8. The stochastic model for simulating the columnar structure solidified under a relatively constant G/V ratio, which is perhaps the most common morphology encountered during secondary remelting processes, was presented for the first time in References 1 and 2.

The importance of modeling the formation of NbC/Laves phases in alloy 718 has been discussed extensively in literature.[15–17] It is also known that the solidification path affects the distribution and amount of carbides and Laves phases in alloy 718. The volume fraction of solid is a function of local growth velocity, solidification time, solidus temperature, and local temperature gradient. The redistribution of elements strongly affects the phase evolution in common superalloys with respect to temperature, as well as their mechanical properties and surface stability at elevated temperatures. The primary goal of this work was to develop a solidification kinetics model for predicting the evolution of NbC and Laves phases during ingot solidification.

Previous studies on alloy 718 showed that both NbC and Laves phases produce intergranular liquid films due to the intergranular distribution of niobi-um and carbon.[16,17] Also, the ability of Laves phases to promote intergranular liquation cracking (microfissuring and hot cracking) during heat treatment is much higher than that of NbC because the temperature for the formation of Laves phases is usually lower than that for NbC (i.e., liquation initiates at the eutectic-Laves temperature). In References 16 and 17, it was demonstrated that the carbon content of alloy 718 directly affects the volume fraction of carbides; the as-cast alloy could contain a higher volume fraction of NbC and Laves phases than what the phase diagram suggests due to the formation of microsegregation during solidification. The relative volume fractions of both NbC and Laves phases depend on the C/Nb ratio. Alloys with a high C/Nb ratio will have a higher volume fraction of carbides than alloys with a low C/Nb ratio.

In developing a solidification kinetics model for predicting the formation of NbC/Laves phases in alloy 718, the following assumptions were made: instantaneous nucleation, carbide growth in the liquid, no interference between growing carbides, carbides are either pushed or engulfed by the S/L interface, volume diffusion-limited growth of carbides, and binary diffusion couple. The stochastic model accounts for nucleation and growth of columnar or equiaxed dendritic grains; growth/remelting of spherical instabilities; nucleation and growth of NbC, assuming that the slowest step is the volume diffusion of carbon from the liquid to the NbC/liquid interface; the redistribution of niobium and carbon concentrations; the redistribution of NbC

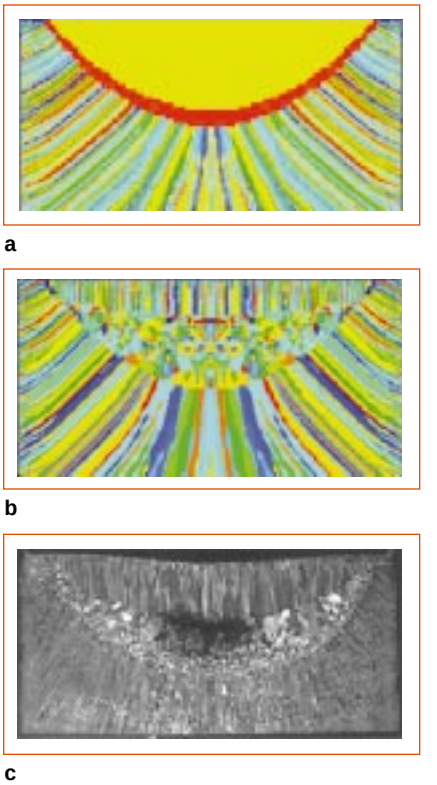

Figure 3. Experimental validation of a VAR model without hot topping (D = 508 mm, 172 kg/h) showing (a) a simulated top ingot structure before stopping the power input, (b) the simulated top ingot structure after stopping the power input and upon complete solidification, and (c) a top-cut section macroetch of an experimental structure.[23]

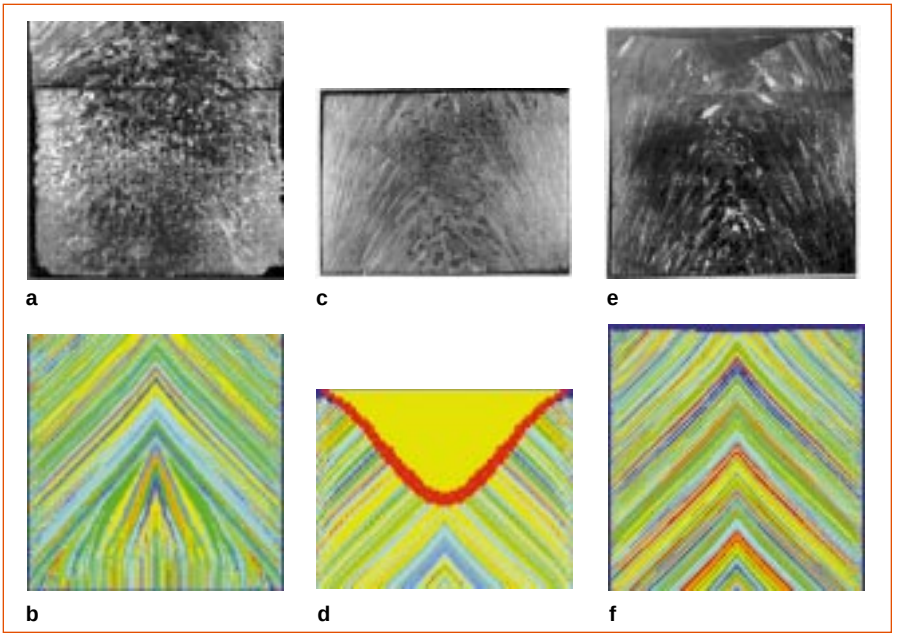

Figure 4. A comparison of calculated and experimental ESR ingot grain structures (D = 432 mm, 272 kg/h, H = 2.1 m, 16 million microvolume elements, CPU time = 10 hours). (a) The experimental initial transient state, (b) the calculated initial transient state, (c) the experimental steady state, (d) the calculated steady state, (e) the experiment final transient state, and (f) the calculated final transient state. The macroetches of the ESR ingot were scanned from Reference 25.

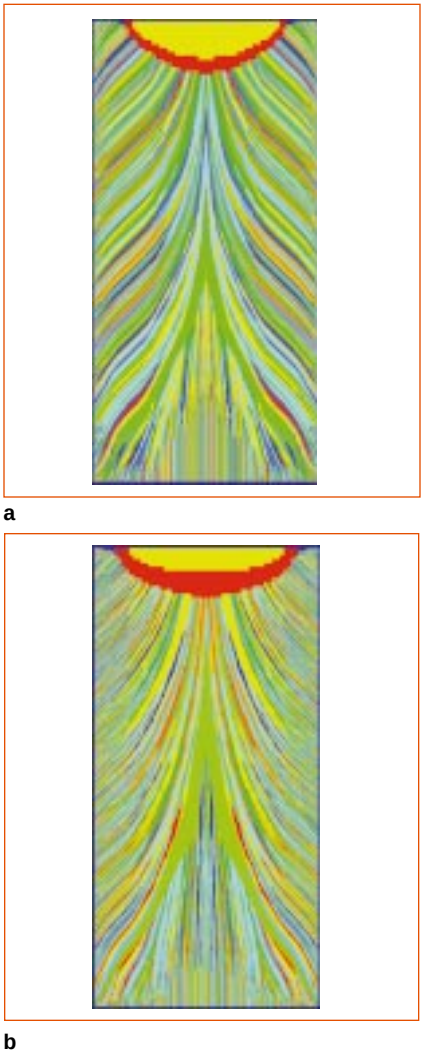

Figure 5. The grain structure formation of VAR alloy 718 ingots (172 kg/h, D = 508 mm) (a) without fluid flow and (b) with fluid flow.

particles between the solid and liquid phases at the level of the secondary arm spacing, taking into account the pushing/engulfment transition; and the nucleation and growth of Laves phases. These features are discussed in greater detail in References 1, 2, 15, 18–22.

THE SIMULATION OF GRAIN STRUCTURES

Grain-growth direction and micro-/macrosegregation-related defects, such as freckles and tree-ring patterns in alloy 718, are directly related to the size and profile of the melting pool. The pool characteristics are mostly controlled by the casting rate and energy input. They are also strongly dependent on the ingot diameter. Grain size and shape, as well as micro-/macrosegregation patterns are strongly influenced by the heat-extraction rate at the metal/mold interface.

Figure 2 shows simulated structures of alloy 718 remelt ingots made by the VAR and ESR processes. The red color represents the mushy zone, the yellow indicates the liquid region (melting pool), and the remaining area shows the solidified grain structure. A total of 255 colors was used in the solid region to illustrate the grain boundary of dendritic equiaxed and columnar structures. The colors also show the crystallographic orientation of columnar grains that have nucleated at the ingot/mold interface. The nucleation and growth competition of columnar grains can be seen in Figure 2. These grains randomly nucleate at the ingot/mold interface and grow toward the ingot center. Note that the grains also grow in a direction opposite to the withdrawal direction (upward solidification), closely following the direction of mushy-region gradients. Steady state in both VAR and ESR processes is achieved when the height of the ingot equals its diameter (H = D).

The simulated ESR ingots contain V-shaped pool profiles with nonuniform, columnar grain size distribution from the ingot center to the outside edge. The simulated VAR ingots have U-shaped pool profiles with relatively uniform, columnar grain size distribution. The grain growth direction in the ESR ingots is between 0 degrees (at the ingot surface) and 45 degrees (at the ingot center) with respect to the ingot vertical axis, while in the VAR ingots, the grain growth direction is between 90 degrees (at the ingot surface) and 0 degrees (at the ingot center). The smaller the growth angle at the ingot center, the lower the tendency is to form the CET. The grain growth direction is mostly controlled by the power input and the power distribution over the top surface of the ingot. As a result, a VAR ingot develops different grain structure than an ESR ingot.

Figure 3 shows comparisons between experiments and simulated results of VAR ingots, cast without hot topping, for a melting rate of 172 kg/h. After the power was shut off, the ingot top region was allowed to solidify in vacuum. Radiative heat loss over the ingot top area was considered in the numerical calculations. The complexity of the ingot structure is shown.

There are three grain morphologies: columnar grains solidified under a relatively constant G/V ratio (the steady-state structure), columnar grains formed under a variable G/V ratio (from the top surface of the ingot), and equiaxed grains. Two transitions also take place: the structural CET and the transition from small-to-large equiaxed grains. The former transition occurs because equiaxed grains nucleate and grow ahead of both columnar fronts. The latter transition occurs because of grain sedimentation or a sudden change in the solidification conditions. In the present model, the CET is driven by a critical-temperature-gradient criterion (i.e., a temperature-gradient value below which equiaxed nuclei may form). The ability and tendency of the equiaxed grains to grow in the mushy region are directly considered in the model through the growth competition between the columnar and equiaxed grains. If equiaxed grain growth is slower than columnar grain growth, columnar growth dominates, and the small equiaxed grains can become stumped and trapped between the columnar grains. This aspect of CET modeling was successfully demonstrated in Reference 8. However, under the present solidification conditions, equiaxed growth is relatively fast compared to the columnar growth, and as soon as the equiaxed nuclei become active, they grow and initiate the CET (Figure 3b). Also, the steady-state columnar fronts (Figure 3a) advance at a much slower rate when compared to the final grain structures (Figure 3b).

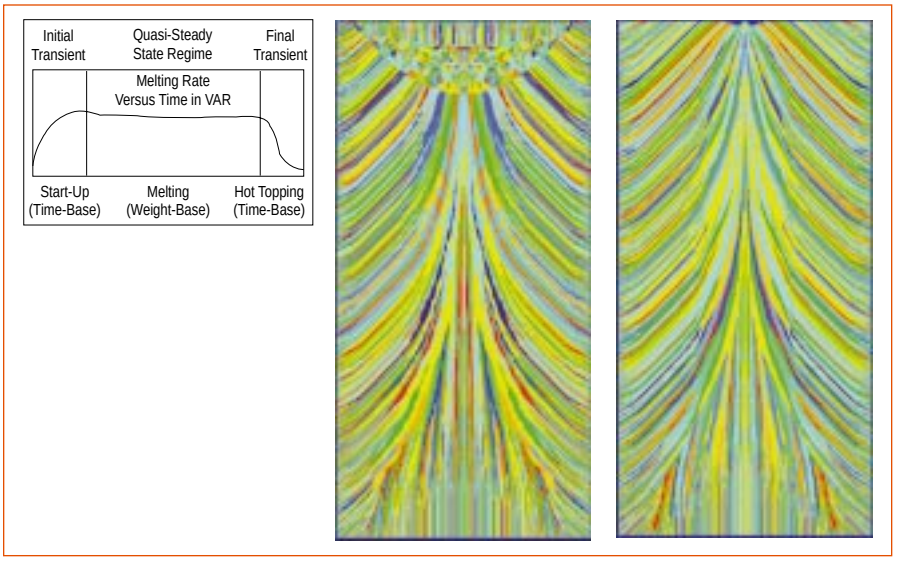

Figure 6. A procedure for the optimization of VAR processes for alloy 718 (172 kg/h, D = 508 mm): (a) a schematic diagram showing the optimum variation of melting rate versus time, (b) a simulated VAR ingot structure solidified without hot topping, and (c) a simulated VAR ingot structure solidified with optimized hot topping.

Overall, micro- and macrostructural particularities, such as grain size, grain structure, grain growth pattern, and CET, are accurately predicted with the present stochastic model. The pool depth and pool profile match very well with the experiments. However, discrepancies in the grain growth direction close to the ingot surface for low melting rates can be observed in Figures 3b and 3c.

Comparisons between simulated results and experimental macrographs[23–25] of ESR ingots for a melting rate of 272 kg/h are shown in Figure 4. The initial transient state is shown in Figures 4a and 4b for simulated and experimental results.[25] The stochastic-model predictions of location and structure in this region are in reasonable agreement with the experiments. Here, the size of the initial transient region equals the ingot diameter.

A comparison between experimental and simulated results after reaching the steady state is presented in Figures 4c and 4d. Although the calculated pool profile and size matched well with the experimental measurements, a small discrepancy exists in terms of grain growth direction. Fluid-flow calculations in the liquid and mushy regions would reduce this mismatch.

Both the experimental and the simulated structures of the ESR top ingots (final transient regimes) are shown in Figures 4e and 4f. The simulated ingot structure in Figure 4f was obtained after power was shut off, and the top region was able to completely solidify. In this case, the slag acts as hot topping because of its insulating capacity. Note that the shrinkage pipe formed at the ingot top region is not simulated with the present model. The model-predicted results, such as pool profile and size, grain growth pattern, and the shape and size of the columnar grains, compared reasonably well with experiments.

The influence of fluid flow on the grain structure formation of VAR alloy 718 ingots is shown in Figure 5. Some differences exist in terms of grain growth direction, grain size, and pool characteristics with fluid flow and without fluid flow.

Hot topping is an important step in reducing remelt processing scrap. Figure 6 shows a comparison of VAR ingot structures obtained without and with optimized hot topping for alloy 718. When the hot topping was simulated, a sigmoidal decrease in the power input was considered, such that the temperature of the ingot top surface was always above the liquidus temperature of the alloy under consideration. This restriction has certainly prevented nucleation and, therefore, grain growth from the ingot top surface. This optimization will increase the ingot yield by reducing the material loss due to the formation of the shrinkage pipe at the top of the ingot.

THE SIMULATION OF SECONDARY PHASES

Correctly calculating the evolution of the secondary dendrite arm spacing (SDAS) is a necessary condition for accurately predicting the formation of the secondary phases in alloy 718 remelt ingots. Figure 7 shows a comparison between calculated and experimental SDAS for VAR and ESR ingots of alloy 718. Two different melting rates are considered for each remelting process. The calculated SDAS agrees closely with the experimental measurements; insignificant differences exist between the ESR and the VAR results in terms of SDAS size. As expected, the SDAS decreases in size when the power input and melting rate increase.

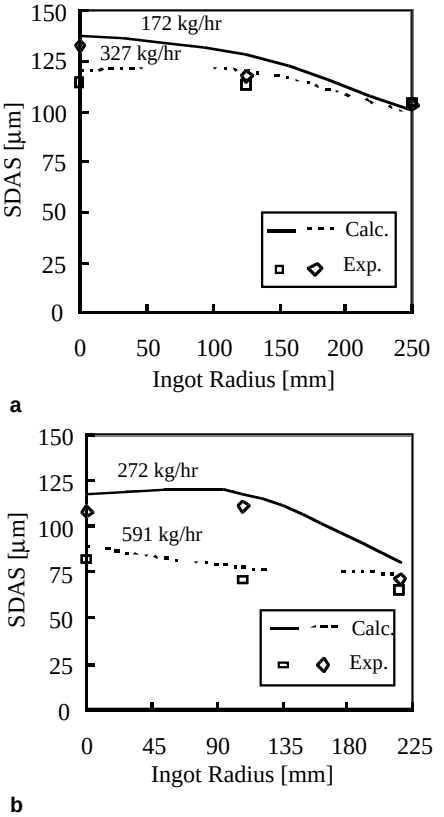

Figure 7. Secondary dendrite arm spacing results for (a) VAR and (b) ESR alloy 718 ingots. Experimental data were taken from Reference 23.

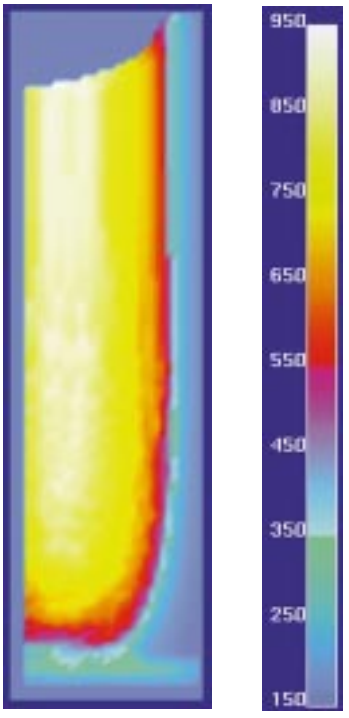

a

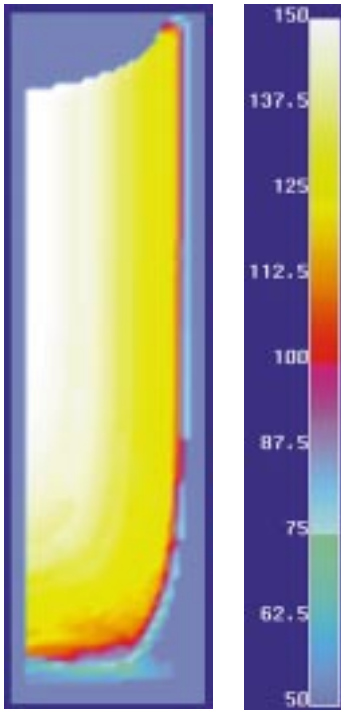

b

Figure 8. Predicted (a) primary and (b) secondary arm spacings in VAR alloy 718 ingots (172 kg/h, D = 508 mm).

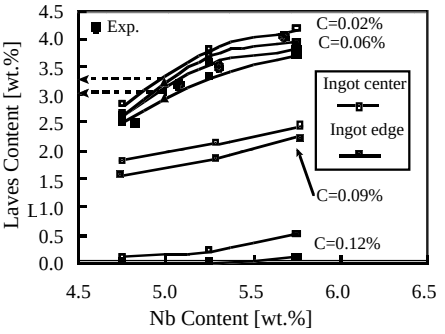

a

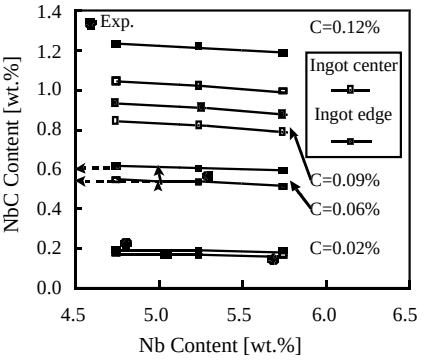

b

Figure 9. The influence of niobium and carbon on the amounts of (a) Laves phases and (b) NbC in VAR alloy 718 ingots (melting rate is 327 kg/h). Data are taken from References 7, 15, 26.

The predicted maps of both the primary and the secondary arm spacings for the VAR alloy 718 ingot (melting rate of 172 kg/h) are presented in Figure 8. The primary arm spacing size varies over the entire ingot between 150 μm and approximately 1,000 μm. It is mostly controlled by the local gradients in the mushy zone and by the solidification rates. The size of the secondary arm spacing changes from 50 μm to 150 μm over the ingot diameter. It is related to the local solidification times or the local cooling rates in the mushy zone.

Figure 9 shows the effects of the cooling rates and initial carbon and niobium concentrations on the amount of NbC and Laves phases precipitated at the interdendritic and intradendritic regions for the VAR alloy 718 ingot (melting rate is 327 kg/h). These results are shown at the steady state for H = 1.5 D. An example calculation, indicated by dotted lines, shows that approximately 3–3.3 wt.% Laves and 0.53–0.6 wt.% NbC would form for a typical initial composition of 5.0 wt.% niobium and 0.05 wt.% carbon. Additionally, the amount of Laves phases formed is strongly dependent on the local cooling rates and initial niobium content and less on the initial carbon content. A similar trend is observed for NbC, in which the amount of precipitated NbC is controlled by the initial carbon content and local cooling rates and less by the amount of Laves phases.

The calculations in Figure 9 reveal that the amount of both NbC and Laves phases is controlled by the combinations of carbon and niobium concentrations and ingot cooling. For instance, in VAR and ESR ingots, an initial niobium content of 4.75 wt.% and a minimum initial carbon content of 0.12 wt.% would result in a Laves-free microstructure with a maximum 1.25 wt.% NbC phase. Also, cooling rates below 5 K/s, as usually encountered in remelt ingots, would favor the formation of low amounts of NbC and Laves phases, and NbC particles would segregate more at the grain boundary. Results from this type of calculation can be useful in understanding the formation tendency of freckle-type defects in VAR and ESR alloy 718 ingots.

Figure 10 presents a complete prediction of the secondary phases in alloy 718 remelt ingots, including morphology, size, amount, and distribution. The simulation was performed on a location close to the ingot center and in the steady-state region. Note that both the NbC and the Laves phases are distributed proximal to the interdendritic region. The amount of secondary phases shown are typical for alloy 718 cast ingots.

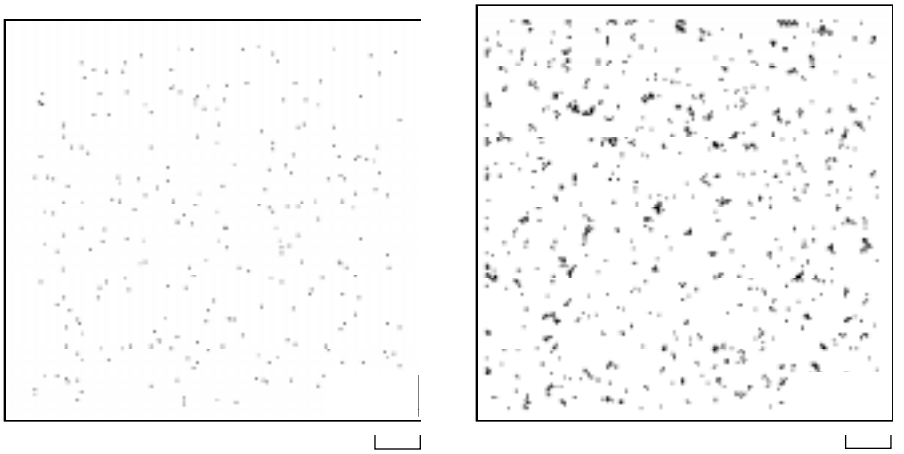

a b

Figure 10. Simulated distribution (1 mm × 1 mm; magnification: 100×) of (a) 0.6 wt.% blocky NbC (5 μm) and (b) 3.16 wt.% globular Laves (5–50 μm); secondary arm spacing is 128 μm in VAR alloy 718 ingots.

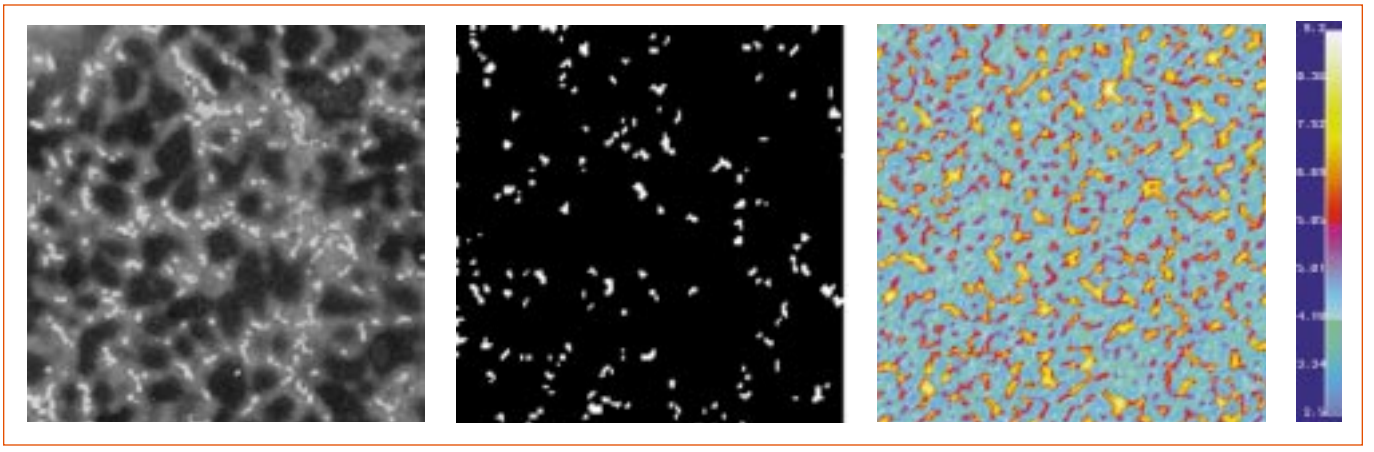

Figure 11. (a) An experimental micrograph showing the Laves distribution as presented by Radavich in Reference 27. (b) Simulated distribution (0.7 mm × 0.9 mm; magnification: 100×) of (b) 3.21 wt.% globular Laves (5–50 μm) and (c) niobium microsegregation for an initial composition of 5.25 wt.% niobium and 0.06 wt.% carbon; secondary arm spacing is 120 μm.

Figure 11 shows another example for niobium microsegregation and distribution of Laves phases. The simulated results in Figures 11b and 11c are compared with the experimental micrograph (Figure 11a) presented by Radavitch in Reference 27 for cast alloy 718. Note that a novel Monte Carlo technique[28–32] was used to calculate the microsegregation of niobium at the level of secondary arm spacing. The use of a probabilistic Monte Carlo technique for microsegregation calculations was required because of the size and complexity of the microstructure in Figure 11.

ACKNOWLEDGEMENTS

This work was conducted by the National Center for Excellence in Metalworking Technology, operated by Concurrent Technologies Corporation under contract number N00140-92-C-BC49 for the U.S. Navy as part of the U.S. Navy Manufacturing Technology Program.

References

1. L. Nastac et al., *Proceedings of the 1997 International Symposium on Liquid Metals Processing and Casting*, eds. A. Mitchell and P. Aubertin (Sante Fe, NM: AVS, 1997), pp. 145–165.
2. L. Nastac, S. Sundarraj, and K.O. Yu, *Proceedings of the Fourth International Symposium on Superalloy 718, 625, 706 and Various Derivatives*, ed. E.A. Loria (Warrendale, PA: TMS, 1997), pp. 55–66.
3. S. Sundarraj et al., *Proceedings of the Modeling of Casting, Welding, and Advanced Solidification Processes VIII* (Warrendale, PA: TMS, 1998).
4. J. Gleick, *Chaos—Making a New Science* (New York: Penguin Books, 1987).
5. COMPACT™ (Minneapolis, MN: Innovative Research)
6. M. Rappaz and Gh.A. Gandin, *Acta Metall.*, 41(2) (1993), pp. 345–360.
7. L. Nastac, Ph.D. dissertation, University of Alabama, Tuscaloosa (1995).
8. L. Nastac and D.M. Stefanescu, *Modelling Simul. Mater. Sci. Eng.*, 5 (1997), pp. 391–420.
9. M.P. Anderson et al., *Acta Metall.*, 32 (5) (1991), pp. 783–791.
10. H.W. Hesselbarth and I.R. Goebel, *Acta Metall.*, 39 (9) (1991), pp. 2135–2143.
11. D.M. Stefanescu, *Modeling of Casting, Welding and Advanced Solidification Processes VI*, ed. T. S. Piwonka et al. (Warrendale, PA: TMS, 1993), pp. 3–20.
12. D.M. Stefanescu and H. Pang, *Proceedings of the International Symposium by the Computer Applications Committee of the Metallurgical Society of CIM*, eds. S.A. Argyropoulus and F. Mucciardi (Montreal: CIM, 1996), pp. 164–176.
13. H. Pang and D.M. Stefanescu, *Solidification Science and Processing*, eds. I. Ohnaka and D. M. Stefanescu (Warrendale, PA: TMS, 1996).
14. G.K. Upadhya et al., *Modeling of Casting, Welding and Advanced Solidification Processes*, eds. M. Cross and J. Campbell (Warrendale, PA: TMS, 1995), pp. 517–524.
15. L. Nastac and D.M. Stefanescu, *Met. Mat. Trans.*, 28A (1997), pp. 1582–1587.
16. B. Radhakrishnan and R.G. Thompson, *Met. Trans.*, 22A (1991), pp. 887–902.
17. C. Chen, R.G. Thompson, and D.W. Davis, *Superalloys 718, 625 and Various Derivatives*, ed. E.A. Loria (Warrendale, PA: TMS, 1991), pp. 81–96.
18. L. Nastac and D.M. Stefanescu, *Met. Mat. Trans.*, 27A (1996), pp. 4061–4074.
19. L. Nastac and D.M. Stefanescu, *Met. Mat. Trans.*, 27A (1996), pp. 4075–4083.
20. L. Nastac and D.M. Stefanescu, *Modeling of Casting, Welding and Advanced Solidification Processes VI*, eds. T.S. Piwonka et al. (Warrendale, PA, TMS, 1993), pp. 209–218.
21. L. Nastac and D.M. Stefanescu, *AFS Trans.* (1996), pp. 425–434.
22. L. Nastac and D.M. Stefanescu, *Met. Trans.*, 24A (1993), 2107–2118.
23. K.O. Yu and H.D. Flanders, *Proceedings of the Vacuum Metallurgy Conference on Specialty Metals, Melting and Processing* (Pittsburgh, PA: AVS, 1984), pp. 107–118.
24. K.O. Yu, *Proceedings of the Vacuum Metallurgy Conference on Specialty Metals, Melting and Processing* (Pittsburgh, PA: AVS, 1984), pp. 83–92.
25. K.O. Yu, internal report, Special Metals Corporation (1982).
26. J.S. Chou et al., private communication, Concurrent Technologies Corporation (1997).
27. J.F. Radavitch, *Proceedings of the Fourth International Symposium on Superalloy 718, 625, 706 and Various Derivatives*, ed. E.A. Loria (Warrendale, PA: TMS, 1997), pp. 17–26.
28. A. Haji-Sheikh and E.M. Sparrow, *J. of Heat Transfer*, 89 (1967), pp. 121–131.
29. A. Haji-Sheikh and F.P. Buckingham, *J. of Heat Transfer*, 115 (1993), pp. 26–33.
30. A. Haji-Sheikh and R. Lakshminarayanan, *Proc. Int. Symp. On Cooling Technology for Electronic Equipment* (Hawaii, 1987), pp. 550–564.
31. T.J. Hofmann and N.E. Banks, *Nuclear Sci. and Engrg.*, 59 (1976), pp. 205–214.
32. A. Haji-Sheikh and E.M. Sparrow, *J. SIAM Appl. Math.*, 14 (1966), pp. 370–389.

ABOUT THE AUTHORS

Laurentiu Nastac earned his Ph.D. in metallurgical and materials engineering at the University of Alabama at Tuscaloosa in 1995. He is currently a senior staff engineer at Concurrent Technologies Corporation. Dr. Nastac is a member of TMS.

Suresh Sundarraj earned his Ph.D. in mineral engineering at the University of Minnesota in 1994. He is currently a process modeling engineer for Concurrent Technologies Corporation. Dr. Sundarraj is also a member of TMS.

Kuang-O Yu earned his Ph.D. in metallurgical engineering at the University of Kentucky in 1978. He is currently director of research and development at RMI Titanium Company. Dr. Yu is also a member of TMS.

Yuan Pang earned his M.S. in mechanical engineering at the University of Akron in 1977. He is currently a principal engineer at Concurrent Technologies Corporation.

For more information, contact L. Nastac, Concurrent Technologies Corporation, 1450 Scalp Avenue, Johnstown, Pennsylvania 15904; (814) 269-2535; fax (814) 269-4458; e-mail nastac@ctc.com.